CORRECTED 8 NOVEMBER 2021; SEE FULL TEXT
SCIENCE ROBOTICS | RESEARCH ARTICLE

MEDICAL ROBOTS

Endoscopy-assisted magnetic navigation of biohybrid soft microrobots with rapid endoluminal delivery and imaging

Ben Wang[1]*, Kai Fung Chan[2]*, Ke Yuan[1,3], Qianqian Wang[1], Xianfeng Xia[2,4], Lidong Yang[1], Ho Ko[5,6], Yi-Xiang J. Wang[7], Joseph Jao Yiu Sung[5,8], Philip Wai Yan Chiu[2,4,8,9], Li Zhang[1,2,9†]

High-precision delivery of microrobots at the whole-body scale is of considerable importance for efforts toward targeted therapeutic intervention. However, vision-based control of microrobots, to deep and narrow spaces inside the body, remains a challenge. Here, we report a soft and resilient magnetic cell microrobot with high biocompatibility that can interface with the human body and adapt to the complex surroundings while navigating inside the body. We achieve time-efficient delivery of soft microrobots using an integrated platform called endoscopy-assisted magnetic actuation with dual imaging system (EMADIS). EMADIS enables rapid deployment across multiple organ/tissue barriers at the whole-body scale and high-precision delivery of soft and biohybrid microrobots in real time to tiny regions with depth up to meter scale through natural orifice, which are commonly inaccessible and even invisible by conventional endoscope and medical robots. The precise delivery of magnetic stem cell spheroid microrobots (MSCSMs) by the EMADIS transesophageal into the bile duct with a total distance of about 100 centimeters can be completed within 8 minutes. The integration strategy offers a full clinical imaging technique–based therapeutic/intervention system, which broadens the accessibility of hitherto hard-to-access regions, by means of soft microrobots.

INTRODUCTION

The field of microrobotics has experienced rapid development; a key aim of the field is localized delivery of tiny robots inside the human body for a variety of biomedical applications, such as drug delivery (*1*–*5*), sensing and diagnosis (*6*, *7*), minimally invasive surgery (*8*, *9*), thrombus ablation (*10*, *11*), and so on (*12*–*15*). In particular, magnetic field–actuated microrobots offer an optimal option toward in vivo applications, owing to their deep penetration and safety features (*16*–*28*). Low-strength magnetic fields are considered harmless to biological cells and with a capability of deep tissue/bone penetration; hence, it is a promising approach for in vivo applications (*15*, *28*, *29*). However, to move forward to biomedical applications, multifunctional microrobots with high safety and adaptability are required. Recently, soft robots demonstrated the ability to interface with the human body, adapt to unpredictable surroundings, and undergo large deformations, based on their inherent structural compliance (*30*–*35*).

Although the targeted delivery of microrobots to several organ-scale tissues and large cavities (*4*, *12*, *13*, *36*), such as the gastrointestinal (GI) tract, has been realized, as listed in table S1, there still exists a variety of regions that are difficult to access by means of microrobots with vision-based control. These regions include the tiny cavities and tortuous ducts located across the blood circulation system and bile ducts, among others, that render the delivery of microrobots to these hard-to-reach regions highly challenging (*37*, *38*). In addition, although a magnetic actuation unit can carry out the high-precision navigation of microrobots, the high-motion precision will inevitably result in a compromise of the delivery range, rendering the whole-body scale navigation of microrobots time consuming. Reports of precisely localized delivery of microrobots with a long distance across the complex and dynamic environment inside the body to the deep and narrow space are limited (*39*). Endoscopy is known for its ability to traverse long distances and rapid deployment in a variety of organs with real-time feedback from endoscopic view. However, endoscopy demonstrates limited accessibility to the deep inside regions within tortuous ducts. To realize rapid and high-precision delivery of microrobots to hard-to-reach regions, one potential strategy is to combine their complementary advantages by integrating the tethered endoscopy and untethered soft microrobots.

Here, we have developed soft and resilient magnetic stem cell spheroid microrobots (MSCSMs) using the three-dimensional (3D) self-assembly of stem cells, doped with a low dose of magnetic particles. The soft and biocompatible MSCSMs show adaptability to the surroundings by self-alternating their structure in a reconfigurable fashion. The stem cells can be harvested from the host so that the immune response can be minimized and even eliminated during MSCSM delivery and therapy. To deliver the microrobots into the deep and narrow spaces inside the body, an integrated robotic platform was developed, termed endoscopy-assisted magnetic actuation with a dual imaging system (EMADIS). In EMADIS, the endoscope offers an "express lane" for the MSCSMs to avoid direct contact with the complex fluidic environments and facilitates the

[1]Department of Mechanical and Automation Engineering, Chinese University of Hong Kong, Hong Kong, China. [2]Chow Yuk Ho Technology Centre for Innovative Medicine, Chinese University of Hong Kong, Hong Kong, China. [3]Department of Biomedical Engineering, Chinese University of Hong Kong, Hong Kong, China. [4]Department of Surgery, Chinese University of Hong Kong, Hong Kong, China. [5]Department of Medicine and Therapeutics and School of Biomedical Sciences, Faculty of Medicine, Chinese University of Hong Kong, Hong Kong, China. [6]Li Ka Shing Institute of Health Sciences, Faculty of Medicine, Chinese University of Hong Kong, Hong Kong, China. [7]Department of Imaging and Interventional Radiology, Chinese University of Hong Kong, Prince of Wales Hospital, Shatin, New Territories, Hong Kong, China. [8]Institute of Digestive Disease, Faculty of Medicine, Chinese University of Hong Kong, China [9]T Stone Robotics Institute, Chinese University of Hong Kong, Hong Kong, China.
*These authors contributed equally to this work.
†Corresponding author. Email: lizhang@mae.cuhk.edu.hk

rapid passage through multiple biological barriers in organs and tissues. The magnetic field actuation guides the high-precision delivery of the MSCSMs to the targeted position after endoscopic deployment. Moreover, the endoscopic view and ultrasound (US) imaging track the entire process. In this way, EMADIS enables the rapid and high-precision delivery of soft microrobots in real time for the targeted therapeutic intervention of hard-to-reach regions, which are inaccessible and even invisible by means of conventional endoscopes and medical robots. The proposed integration strategy offers a full clinical imaging technique-based therapeutic/intervention system, with a highly extended working distance, improved time efficiency for targeted delivery, and diverse functionalities with high clinical value.

RESULTS

System design

We have developed a system that combines the endoscope, US imaging, and soft microrobots to achieve imaging-guided delivery of microrobots to hard-to-reach regions (Movie 1). The advantages of the system, compared with previous works, are that it can precisely deliver the microrobots toward the lesion in an organism at the superficial tissue level or to the deep organs, including large cavities or narrow ducts. Figure 1A gives a typical example of the system, termed EMADIS, that comprises a magnetic actuation platform, an endoscope unit equipped with a catheter, and a US imaging modality. The microrobots can be remotely injected in a controlled and minimally invasive manner to a region located close to the targeted site (Fig. 1B). The subsequent navigation of the microrobots will then rely on magnetic actuation, with real-time tracking, by means of the endoscopic view (Fig. 1, C and D). The tethered endoscope shows a limited accessible region inside the organism, and the untethered microrobots released from the endoscope substantially extend the treatment area of the system. Although the targeted site is hidden in an inaccessible and invisible region by the endoscope, the microrobots can be further tracked by the US imaging technique to reach the destination for therapeutic purposes, lastly, including inside narrow ducts and confined cavities (Fig. 1E). On the basis of the combined platform, we realize the remote and deep-site delivery of microrobots with high-precision and rapid-delivery features. Although the conventional endoscope has demonstrated its capability to access a considerable part of the organism, the proposed EMADIS system further broadens the function and access region of the robot unit to the tortuous and tiny lumens inaccessible and even invisible to an endoscope. The translational speed of MSCSMs inside the endoscopy is two orders larger than that under magnetic actuation. Therefore, maximizing the deployment distance by endoscopy toward the targeting site can shorten the time required for the whole delivery process by the EMADIS. It is notable that although the developed microrobot is a soft MSCSM, the EMADIS is also applicable to other types of microrobots with various functions for rapid delivery.

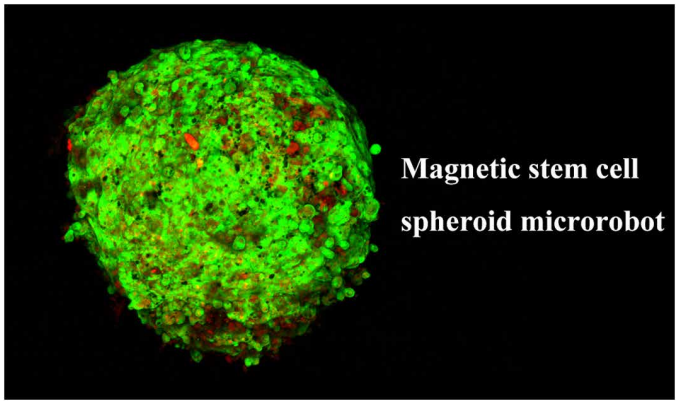

Movie 1. Overview of microrobotic delivery platform. Rapid endoluminal delivery of stem cell spheroid microrobots using endoscopy-assisted magnetic actuation with a dual imaging system.

Fabrication of soft microrobots

The microrobots are fabricated through a coculture process of stem cells and polydopamine (PDA)–coated magnetic iron particles on a nonadhesive surface, forming the spherical structure, as shown in Fig. 2A. Benefitting from the biocompatible PDA shell on the magnetic particles (figs. S1 and S2), the stem cells and the magnetic particles will spontaneously assemble and form a biohybrid tiny agent with spherical shape through a simple coculture process, as indicated by the scanning electron microscopy (SEM), bright-field (BF) microscopy, and confocal laser scanning microscopy (CLSM) images in Fig. 2B and figs. S3 and S4, respectively. The spontaneously formed spherical structure facilitates the magnetic actuation capability. After the cutting process of a typical MSCSM, the inner distributions of stem cells and magnetic particles (2 to 3 μm) were inspected by SEM (Fig. 2C and fig. S5). SEM and transmission electron microscopy (TEM) images in fig. S1 show the morphology and core-shell structure of the magnetic particles. The magnetic saturation value is 198 electromagnetic units (emu)/g (hysteresis value is about 5 emu/g; fig. S1), which is more than twice the magnetic saturation value of commonly prepared magnetite nanoparticles (*40*). The high saturation magnetization of the particles facilitates the remote actuation of the soft microrobots even under a highly viscous environment inside the body. The excellent magnetism facilitates the efficient actuation and delivery of stem cells with an ultralow dose of magnetic particles. To determine the optimal ratio of the magnetic particles in the microrobots, we changed the initial cell concentration and the dose of the magnetic particles to fabricate different types of MSCSMs. The spheroid microrobots remained stable and closely packed at the relatively low particle dose but became unstable when the particle dose exceeded about 0.02 mg (Fig. 2E). The high particle dose is disadvantageous for the formation of the MSCSMs, given that the particles weakened the interactions between the stem cells. The size of the MSCSMs is mainly determined by the initial stem cell concentration (Fig. 2, D and F). The volume percentage of the stem cells in a typical MSCSM (cell number = 100,000; particles amount = 10 μg) was calculated to be about 98.1%, demonstrating the ultralow number of magnetic particles inside the MSCSMs. The cell viabilities of the MSCSMs were verified by the 3-(4,5-dimethylthiazol-2-yl)-5-(3-carboxymethoxyphenyl)-2-(4-sulfophenyl)-2H-tetrazolium (MTS) assay. The dose of magnetic particles had no substantial effect on the cell viability [reflected by the optical density (OD; absorbance) in Fig. 2G] on the MSCSMs when the particle dose was lower than 0.02 mg. The cell viability of MSCSMs increased with increasing initial cell number (Fig. 2G). However, the cell viability remained constant after the initial cell number of 100,000. The possible reason is the hypoxia condition of the inner cells triggered by the large size of MSCSMs.

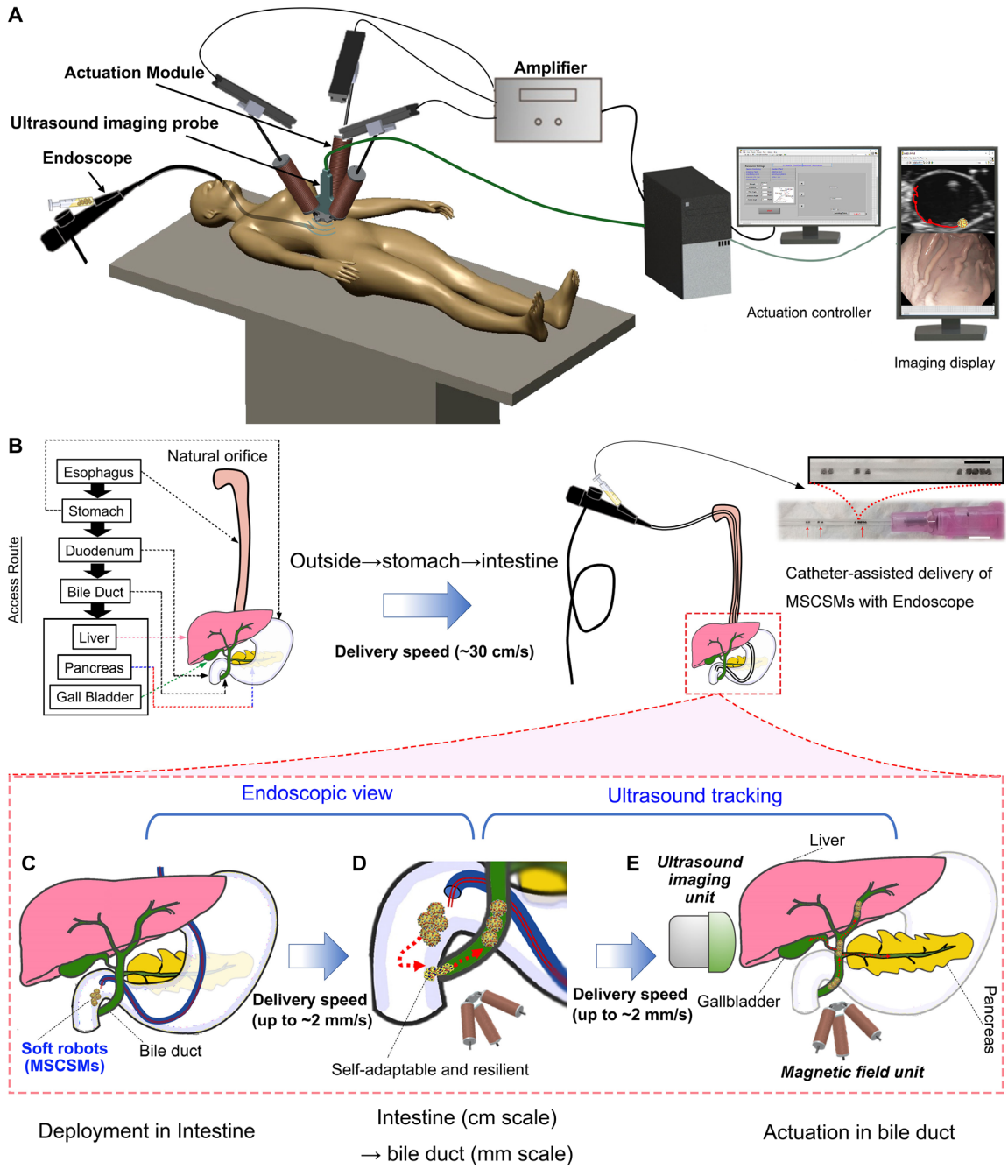

Fig. 1. Combination of endoscopy, US imaging, and soft microrobots for active and rapid delivery to deep and narrow space at the whole-body scale within minutes. (**A**) Conceptual drawing showing the endoscope and US imaging–guided delivery of soft microrobots (i.e., MSCSMs) for targeted therapy in hard-to-reach regions. (**B** to **E**) Schematic showing an example of the active delivery process to the difficult-to-access bile duct. (B) Manipulation of the endoscope from outside to the stomach and finally arriving at the intestine. The inset shows a photograph of the catheter-based delivery of soft microrobots (delivery speed of about 30 cm/s) with controlled numbers. Scale bars, 2 mm (for upper right corner) and 5 mm (for lower right corner). (C) Rapid deployment of the soft microrobots to the intestine through the catheter equipped inside the endoscope. (D) Magnetic actuation of the soft microrobots from the intestine to the entrance of the bile duct under the real-time endoscopic view (delivery speed is about up to 2 mm/s). When the soft microrobots arrive at the entrance site, a strong magnetic field is applied to pull the microrobots into the bile duct in a self-adaptable and resilient fashion. (E) In the bile duct, the soft microrobots are actuated under real-time US imaging of multiple organs.

The neglectable cytotoxicity of the magnetic particles is also verified in figs. S6 and S7. The MSCSMs can be stored in batches for further use, with high cell viability, via a dynamic rotating culture system (fig. S8).

The MSCSMs exhibit elasticity and softness and can be actuated to pass through complex environments in a reconfigurable manner (Fig. 3A). Although the MSCSMs can be compressed on demand (Fig. 3B), they can also recover their shape after the compression is retracted (Fig. 3C). The storage modulus and loss modulus were measured to be about 2.0 and 0.2 kPa, respectively (Fig. 3D). Compared with the common biological samples (*41*, *42*), the modulus of

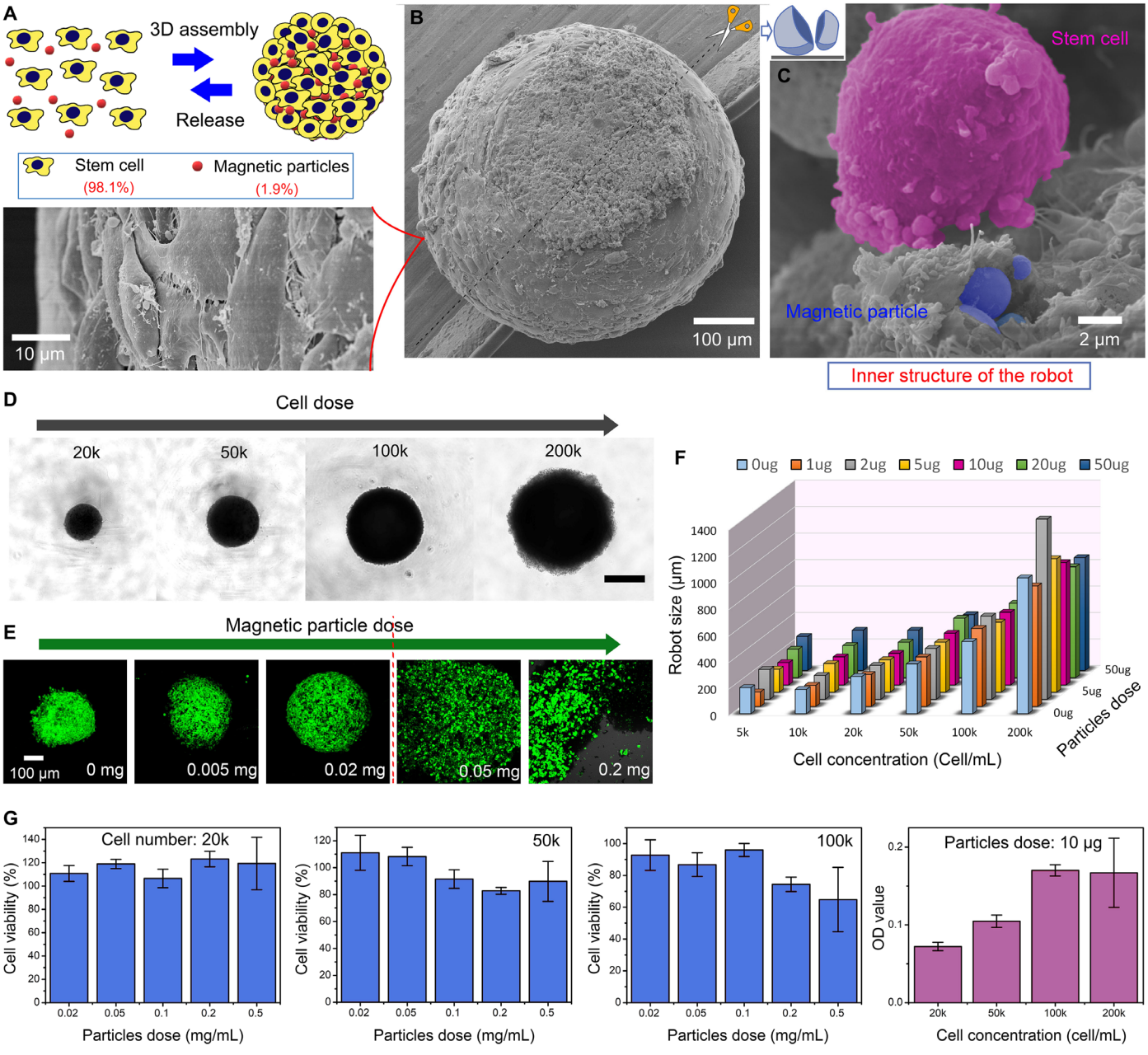

Fig. 2. Fabrication, characterization, and viability assessment of live stem cell spheroid microrobots. (**A**) Schematic showing the self-assembly process of stem cells and magnetic particles into a 3D MSCSM. (**B**) SEM images showing the integral and enlarged views of a MSCSM. (**C**) SEM image showing the inner distribution of the stem cells (pink) and the magnetic particles (blue). (**D**) BF images showing the as-prepared MSCSMs with various initial cell numbers, that is, 20,000 cells, 50,000 cells, 100,000 cells, and 200,000 cells. Scale bar, 500 μm. (**E**) CLSM images showing the morphologies of MSCSMs containing different amounts of magnetic particles. (**F**) Bar graph showing the sizes of MSCSMs with different initial cell numbers and different amounts of magnetic particles. (**G**) Cell viabilities of MSCSMs with different concentrations of magnetic particles. The initial cell numbers are 20,000, 50,000, and 100,000, respectively. OD (absorbance) of MSCSMs with 10-μg magnetic particles and different initial cell numbers. The error bars are obtained from SD of four groups of samples.

the MSCSMs is comparable with that of brain tissue (Fig. 3E), indicating the softness of the MSCSMs. When a soft MSCSM passes through a channel with a smaller width than the diameter of the MSCSM, the MSCSM transforms its shape to adapt to the gap and passes through it in a reconfigurable manner. For a channel with an inner width of about 300 μm, the MSCSM (size is ~500 μm) can recover its shape after passing through the gap (Fig. 3F). A further decrease in the channel width to 200 μm will induce an irrecoverable shape of the MSCSM (Fig. 3F). At the same time, the MSCSM remains intact and maintains its cell viability.

The structure and component of the MSCSMs can be further adjusted by the differentiation and the coculture of multiple MSCSMs. The CLSM images in fig. S9A show that the existence of the magnetic particles in the MSCSMs did not induce substantial

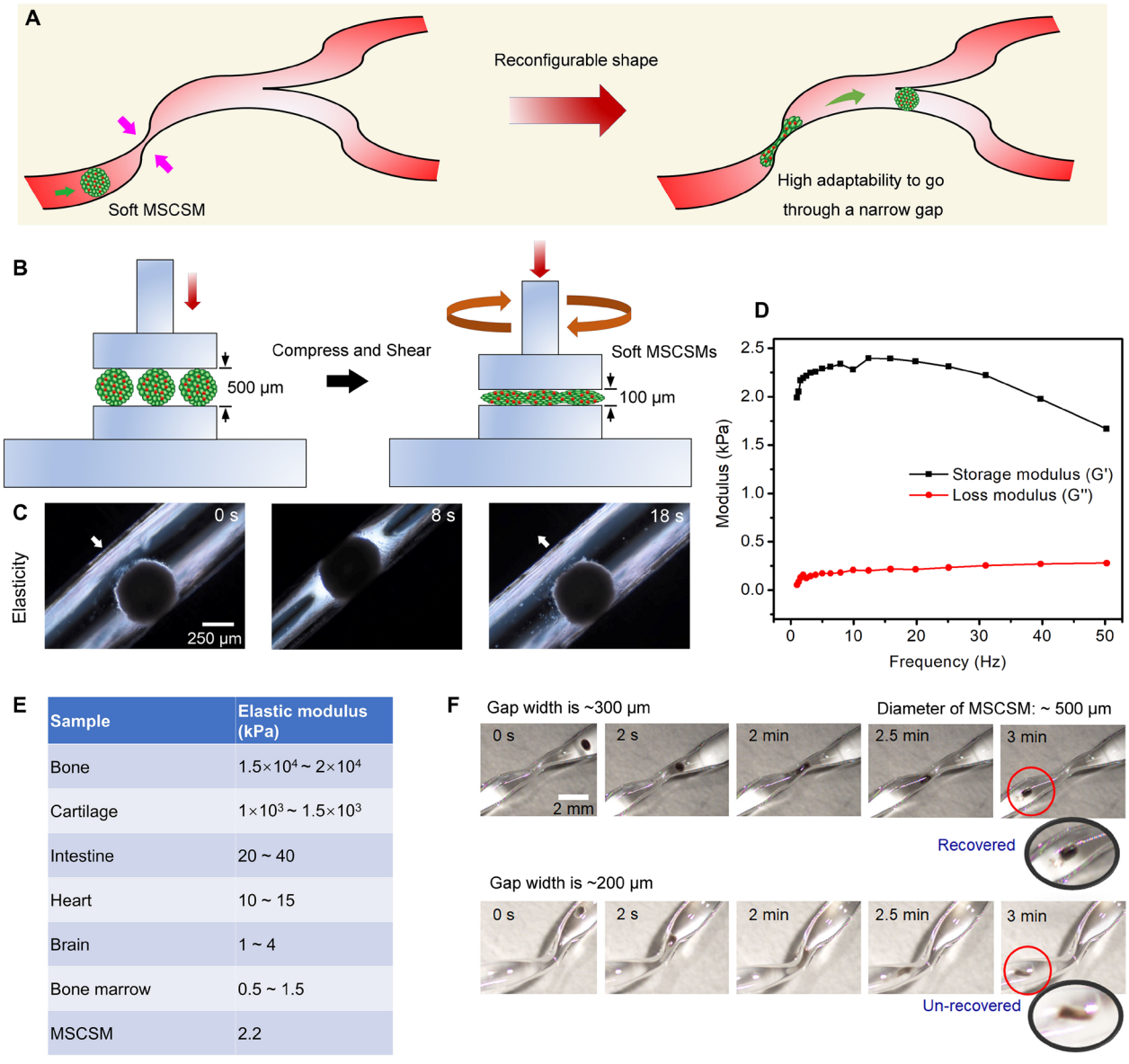

Sample	Elastic modulus (kPa)
Bone	1.5×10^4 ~ 2×10^4
Cartilage	1×10^3 ~ 1.5×10^3
Intestine	20 ~ 40
Heart	10 ~ 15
Brain	1 ~ 4
Bone marrow	0.5 ~ 1.5
MSCSM	2.2

Fig. 3. Softness and elasticity of MSCSMs. (**A**) Schematic showing the reconfigurable motion of the MSCSM while passing through a narrow channel with a width smaller than the diameter of the MSCSM. (**B**) Schematic showing the compression and shearing of the MSCSMs using rheometer (diameter of 500 μm and stage gap of 100 μm). (**C**) Microscopic images showing the compression process of an MSCSM. The shape of the MSCSM recovered after the retraction of the compression. (**D**) Storage modulus (G′) and loss modulus (G″) as functions of frequency. (**E**) Table showing the typical elastic moduli of the human tissues/organs. (**F**) Optical images showing the deformation of the MSCSM when it passes through narrow gaps with different widths through capillary pressure, indicating the high softness and resilience of the MSCSMs.

hypoxia to the stem cells compared with the pure stem cells spheroid, indicating high cell viability of the MSCSMs (cell concentration is 100,000 cells/ml). The high cell viability and low hypoxia of the MSCSMs are crucial for differentiation of the MSCSMs (fig. S9B). The result of in vitro differentiation indicated that released stem cells could differentiate into chondrocytes and osteoblasts (fig. S9, C and D), thereby retaining their potential of multilineage differentiation, and the MSCSMs are able to be converted into other types of cell spheroid microrobots by varying the differentiation factor. The results demonstrated that the component (i.e., cell) of the robots could be adjusted by the differentiation process. In addition, coculture of MSCSMs with a spheroid of another cell type can be adopted to adjust both the component and the geometry of the tiny robots.

Here, we applied 3T3 cell spheroid as an example. The result showed that the MSCSM fused with 3T3 cell spheroid to form a hybrid magnetic cell spheroid microrobots (fig. S10A). Depending on the time of culture, the formed hybrid MSC/3T3 spheroid microrobots have different morphologies and degrees of fusion (fig. S10B). The hybrid MSC/3T3 spheroid microrobots showed a structural Janus form after being cultured for 1 day, which was a dumbbell-shaped microrobot (fig. S10B). On day 3, the MSCSM integrated more with the 3T3 spheroid, forming a componential Janus form (fig. S10B). After 7 days of culture, the MSCSM fused entirely with the 3T3 spheroid, forming a uniform and spherical structure with two types of cells (fig. S10B). The developed cell spheroid robots verified that both structural and componential

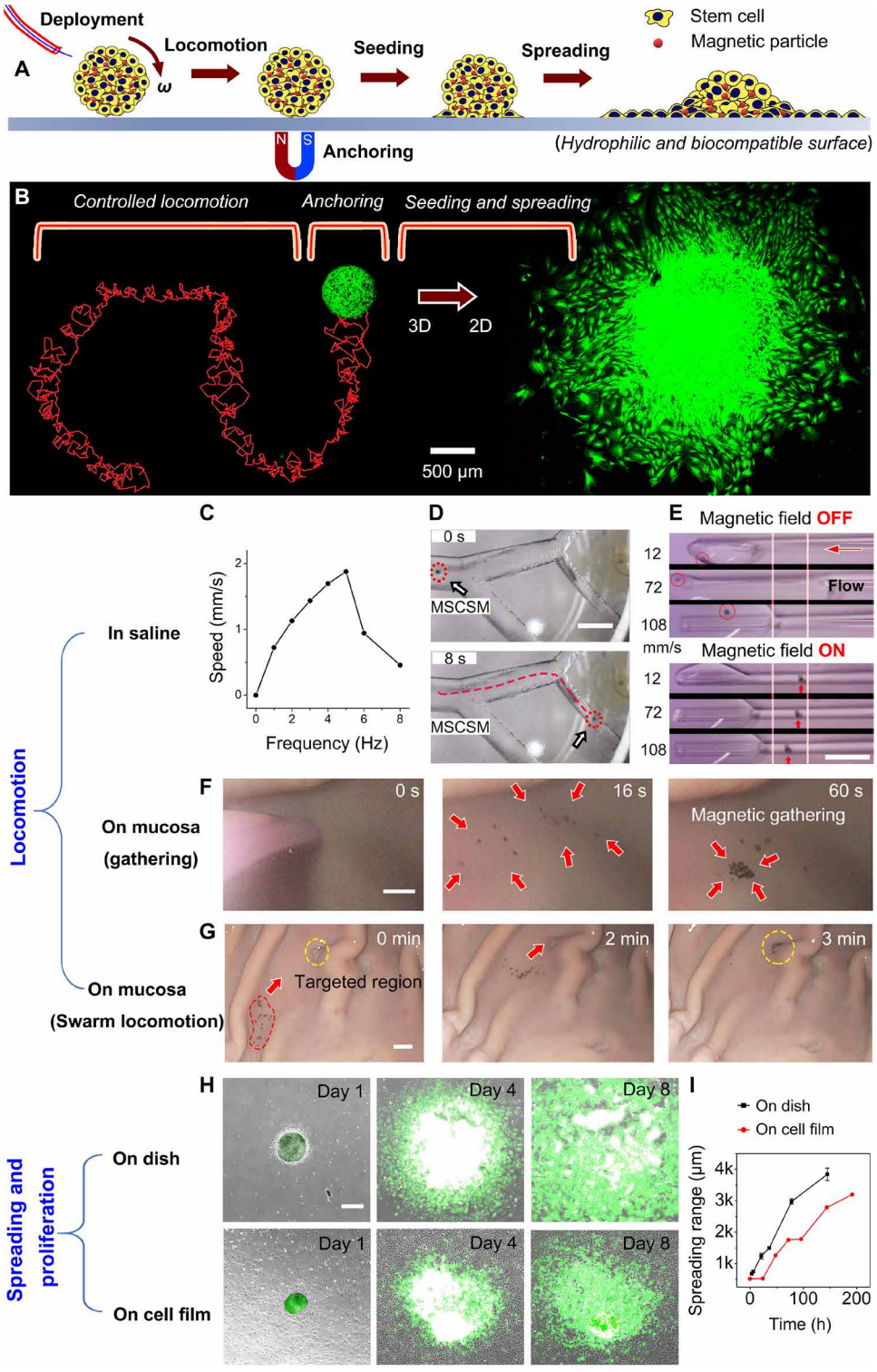

Fig. 4. Controlled locomotion and spreading of MSCSMs over varied surfaces. (**A**) Schematic showing the catheter-based deployment, controlled locomotion, anchoring, seeding, and spreading of the soft microrobots. (**B**) A demo showing the magnetic locomotion of a soft MSCSM (in saline) with a programmable trajectory, anchoring with a magnet, and the spreading of the MSCSM from 3D to 2D (see movie S2). (**C**) Relationship between the speed of the MSCSMs and the input frequency of the magnetic field (field strength is 10 mT, and pitch angle is 90°). (**D**) Successive optical images showing the magnetic locomotion of a MSCSM in a 3D channel (field strength is 10 mT, pitch angle is 90°, and input frequency is 3 Hz). (**E**) Anchoring of the MSCSMs against various flow speeds (up to 108 mm/s) at a specific position. (**F**) Gathering of multiple MSCSMs on mucosa under magnetic field. (**G**) High-precision locomotion of multiple MSCSMs on the uneven mucosa to a premarked position (see movie S4) (**H**) Photographs showing the spreading and proliferation of the MSCSMs on a petri dish and on a 3T3 cell film, respectively. (**I**) Relationships between the spreading range and the incubation time for the on-dish and on-cell cases. Scale bars, 5 mm (D to G) and 500 μm (H). Error bars indicate the SD for $n = 3$.

diversity could be adjusted in a programmable manner from differentiation and coculture strategies.

Controlled locomotion and spreading over varied surfaces

We investigated catheter-based deployment, controlled locomotion, anchoring, seeding, and spreading of the soft microrobots over varied surfaces (Fig. 4A). As illustrated in Fig. 4B, the soft MSCSMs can be navigated with high precision under magnetic field with programmable trajectory "CU," and after anchoring by a magnet for about 3 hours, the spreading and proliferation of the MSCSM from a 3D sphere to a 2D film-like construction can occur spontaneously under a simple incubation process at 37°C. In addition, we investigated the potential aggregation of the magnetic particles at different stages. The results in fig. S11 indicated that the particles showed no obvious aggregation before and after magnetic actuation and after the digestion of the MSCSMs. The magnetic locomotion of the MSCSMs was systematically investigated in the saline environment and the uneven mucosa of stomach. Figure 4C shows the actuation of MSCSMs in saline with different magnetic field frequencies. The maximum speed was measured to be 1.9 mm/s with a step-out frequency of 5 Hz (field strength is 10 mT; see movie S1). The designed MSCSMs can navigate on complex surface topographies containing a series of surfaces and curvatures owing to its spherical shape (Fig. 4D). The cells in the MSCSMs are quite stable during the long-time navigation. As shown in fig. S12, after 1 hour of actuation, the remaining fluorescent intensity of the MSCSM can still reach 89.2% of its initial intensity (see movie S2). In addition, after arriving at the desired

position, the MSCSMs can be fixed to the position, on-demand, against strong flows of up to 108 mm/s (Fig. 4E).

We also investigated the motion property of the MSCSMs under varied viscosities with mucus and interfacial wettabilities. During the navigation of MSCSMs inside the GI tract or other lumens inside the body, the MSCSMs may locate on the surface of mucus or in the mucus. Both cases are considered as shown in fig. S13. For both situations, the translational speed gradually decreased with the increase of the mucus viscosity, whereas the speed decreased with the decrease of the applied magnetic field frequency. While the other parameters are fixed, the translational speed, for the on-mucus case, is slightly higher than the speed of MSCSMs in mucus. In addition, we studied the motion of the MSCSMs on the surfaces with different wettabilities, varying from hydrophilic to hydrophobic surfaces. The translational speed of the MSCSMs shows slight fluctuation in a narrow range (fig. S14), indicating that the surface wettability does not have a substantial influence on the translational speed of MSCSMs.

To further verify the locomotion capability of the MSCSMs on biological tissues/organs, we deploy a group of MSCSMs via transcatheter to the mucosa of pig stomach. With the magnetic field control, the MSCSMs can be gathered (Fig. 4F) and can be actuated with high precision in swarm locomotion toward a premarked targeting region on the mucosa surface (Fig. 4G and fig. S15 and see movie S4). The soft MSCSMs are also capable of performing adaptive seeding, spreading, and proliferation into 2D configurations on cytophilic surfaces as shown in Fig. 4H, which facilitates and boosts the degradation when they are applied for therapeutic applications inside the body. To simulate the interaction of the soft MSCSMs with the cells inside the body, we quantitatively investigated the spreading and proliferation process of the MSCSMs on a cell film. The spreading and proliferation on a petri dish were applied as the control group. As shown in Fig. 4H and figs. S16 and S17, the spreading and proliferation of a MSCSM on the 3T3 cell film can be well performed by an incubation process. The size range of the spread MSCSM shows a linear increase with time (Fig. 4I). The spreading speed of the MSCSMs on the cell film is comparable to that on the petri dish, as illustrated in Fig. 4I. The result denotes that the soft MSCSMs may require no further treatment process after the in vivo therapeutic application because they are able to transform into individual live cells spontaneously on cell/tissue surfaces. The microscopic images in figs. S18 to S20 show the configurations of an MSCSM and two adjacent MSCSMs after the spreading, respectively. The local details suggest that the cells of the MSCSMs migrated outward, and the configuration of cells at the outer ring changed from an irregular shape to a spreading shape (Fig. 4H and figs. S16 and S17).

EMADIS for image-guided delivery to tortuous and tiny lumens

Endoscopy is not only an intensively used clinical imaging technique but also a common surgical tool. The conventional endoscope is a diagnostic tool for vision-based examination of the internal organs, which enters the human body via natural orifices. It can be applied in a variety of organs, including GI tract, respiratory tract, urinary tract, and female reproductive system. Despite the wide range of applications, endoscopy still has several shortcomings, including limited accessibility to hard-to-reach regions and lack of therapeutic tools. For delivery to tortuous and tiny lumens with a long travelling distance up to ~1 m, the combined platform (EMADIS)— comprising an endoscope, magnetic actuation unit, and US imaging setup (Terason t3200, Teratech Corporation, USA)—enables the rapid deployment and high-precision delivery of soft MSCSMs in real time to hard-to-reach regions. Therein, the US imaging–guided actuation of a single MSCSM and multiple MSCSMs in vitro and navigation of a swarm of MSCSMs in vivo have been systematically investigated as given in Supplementary Text (fig. S21 and movie S3). The spatial resolution of our US imaging is about 500 μm, with a penetration depth in the range of 2 to 5 cm. Here, we used the bile duct as an example for demonstration of the rapid delivery of the MSCSMs by the EMADIS. The bile duct is an essential channel (with a diameter of 0.4 to 0.8 cm) that connects the duodenum with the liver, spleen, and gallbladder (Fig. 5A). We used the developed EMADIS to realize the minimally invasive peroral delivery of the MSCSMs into the bile duct precisely by means of magnetic control with real-time feedback from the combined imaging mode of endoscopy and US tracking. The delivery of MSCSMs by the EMADIS can be divided into four stages (Table 1). In stage 0 (Fig. 5B), the MSCSMs were deployed to the duodenum, close to the stomach using the catheter with real-time monitoring by means of the endoscope (Fig. 5C). Here, the inner diameter of the catheter equipped in the endoscope was 2 mm, indicating a capability to deploy tiny robots with a size smaller than 2 mm. Subsequently, under endoscopic monitoring, the released MSCSMs were actuated by a remote magnetic field toward the tiny entrance of the bile duct on the inner wall of the duodenum (stage 1; Fig. 5, D and E). Then, strong magnetic attraction was applied to pull the MSCSMs into the bile duct (stage 2; Fig. 5, D and F). The generated field strength was about 60 mT at the position around the entrance of the bile duct. After the MSCSMs entered the bile duct, the endoscope was unable to observe and track their trajectories (Fig. 5F), and the US imaging setup was switched on for further tracking and guidance of the translational motion of the MSCSMs (stage 3; Fig. 5G). As shown in Fig. 5H, after switching the imaging mode in the bile duct, the MSCSMs can be magnetically driven to the gallbladder with real-time location feedback from the US imaging. The motion distance and time during each stage were estimated, as shown in Table 1. The delivery distance of MSCSMs reached 100 cm during the entire process. However, the time spent on delivery can be controlled to be less than 8 min, demonstrating the time-efficient delivery across extended distances and multiple organ barriers. As shown in the table, the speed of the MSCSMs inside the catheter of the endoscope can reach about 30 cm/s, which is two orders of magnitude higher than the maximum speed when the MSCSMs are under magnetic actuation. Therefore, maximizing the deployment distance by endoscopy is favorable to shorten the time required for the entire delivery process to be completed by means of the EMADIS. High-precision magnetic actuation will then be performed after maximizing the reachable region of endoscope toward the targeted location. The regions that our approach can be applied to are proposed in table S2—including the pancreatic duct, common bile duct, common hepatic duct, intrahepatic bile duct, ureter, and fallopian tube—and the cavity sizes of these regions are specified. The size of residual particles is much smaller than that of the proposed delivery regions, such as common bile duct and intestine (4 and 50 mm, respectively). The residual magnetic particles can pass through these lumens and not induce blockage with ease. The combination of magnetic actuation, endoscopy, and US imaging modality offers the

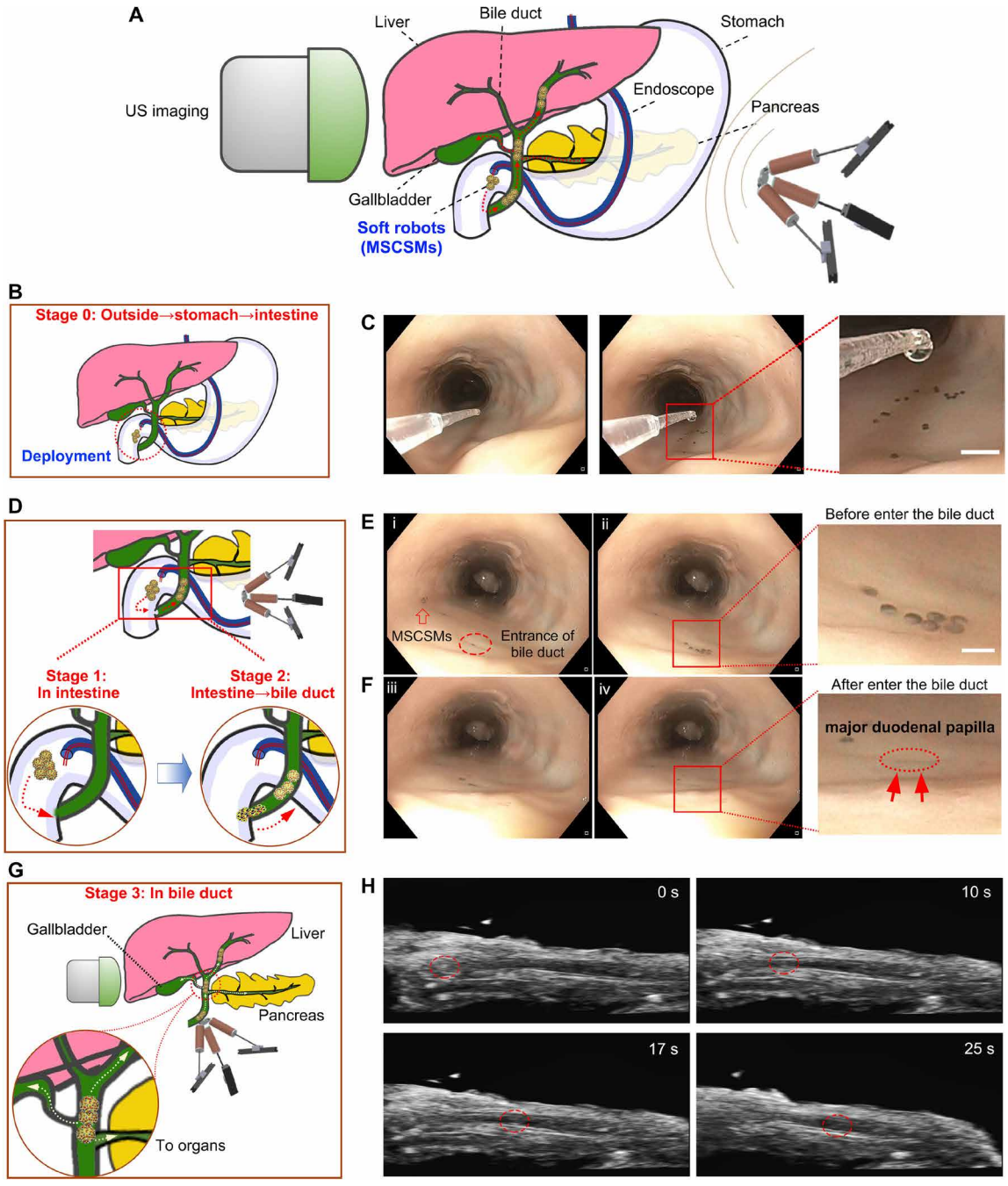

Fig. 5. EMADIS enables the rapid delivery of soft MSCSMs to the bile duct via a natural orifice under combined imaging modalities in real time (movie S5). (**A**) Schematic illustrating the experimental setup. (**B**) Schematic of stage 0. (**C**) Stage 0: Delivery of the MSCSMs by the catheter equipped on an endoscope through the throat to the stomach and finally reaches the intestine. Scale bar, 5 mm. (**D**) Schematic of stages 1 and 2. (**E**) Stage 1: Actuation of MSCSMs toward the entrance of the bile duct under real-time tracking of the endoscope. Scale bar, 1 mm. (**F**) Stage 2: Magnetic attraction of MSCSMs into the bile duct. (**G**) Schematic of the stage 3. (**H**) Stage 3: Magnetic navigation of the MSCSMs inside the bile duct under real-time tracking of US imaging.

maximum application scope of magnetic microrobots for in vivo applications at the whole-body scale (see movie S5).

In addition, we verified the feasibility of the magnetic field–guided delivery of prepared MSCSMs to organs and tissues using magnetic resonance imaging (MRI) as illustrated in Supplementary Text and fig. S22. Figure S22 demonstrates that the swarm of MSCSMs, in both the stomach and abdominal cavity, could be tracked by means of T2-weighted MRI under magnetic actuation. Compared with other types of imaging modalities, MRI is also an excellent candidate for microrobot tracking in deep tissue (table S3). Unlike US imaging, MRI is also applicable for those regions shielded by bone. Therefore, the integration of endoscopy and MRI techniques may provide another potential integrated delivery system for delivery to deep regions.

Table 1. Table showing the steps of the image-guided delivery processes of MSCSMs toward the bile duct by EMADIS. The delivery process can be divided into four stages corresponding to Fig. 5. The deployment/delivery distance at each stage and the time spent are recorded accordingly.

	Process	Imaging mode	Actuation mode	Distance	Time
Stage 0	Endoscope passing through esophagus and stomach, and finally arriving at the intestine	Endoscopy	Endoscopic access	90 cm	30 s
	Microrobots deployment through the catheter and arriving at the intestine			90 cm	5 s
Stage 1	Magnetic navigation of MSCSMs in intestine toward the orifice of bile duct	Endoscopy	Magnetic field	<5 cm	~1 min
Stage 2	Magnetic delivery of MSCSMs into the bile duct (from intestine to bile duct)	Endoscopy	Magnetic field	<1 cm	~1 min
Stage 3	Targeted delivery of MSCSMs in bile duct	US imaging	Magnetic field	~5 cm	~1 min

In vivo localized therapy using MSCSMs

To demonstrate the therapeutic potential of MSCSMs, we have demonstrated their therapeutic effect in both the in vitro repairing of the scratched area (fig. S23) and the in vivo enhancing of the healing of the gastric ulcer in rats. As illustrated in figs. S23 and S24, both the engraftment and secretome of the MSCSMs have been demonstrated to show the repairing effect in the in vitro cases. To perform the in vivo treatment of gastric ulcer in rats, two gastric ulcers with identical initial sizes on the anterior and posterior walls of the stomach were induced by flowing acetic acid burning of the mucosa for 1 min. Then, 30 MSCSMs in 50 μl of saline were injected into one of the ulcers, and 50 μl of saline was injected into another ulcer as the control (Fig. 6). The experiment results indicate that the therapeutic group with MSCSMs injected had a higher healing rate than that of the control group after 3 days (Fig. 6B). The average ulcer area of the MSCSM group after 3 days was 47.141 mm^2, whereas that in the control group was 57.477 mm^2, indicating that the MSCSM group was smaller than the control group ($P < 0.05$). The results suggested that the MSCSMs had a therapeutic effect due to living building blocks inside, i.e., stem cells, which accelerated the healing of the mucosa of the rat's stomach. To testify the engraftment of stem cells in the recovered ulcer region, we euthanized the mice after 3 days of injection to harvest the stomach for histological examination (Fig. 6, C and D). Hematoxylin and eosin (H&E) staining was used to stain the histological slides. Microscopic investigation showed the in vivo engraftment of MSCSMs and the survival of stem cells in the submucosa (Fig. 6C). The fluorescent image (FI) in Fig. 6D shows the released and spread stem cells from the MSCSMs. In addition, no tissue damage was observed in the stomach tissue from the histopathological evaluation. These findings show that the MSCSMs retained the ability of in situ engraftment. Last, we measured the biodistribution of the magnetic particles used in MSCSMs at different time points in healthy rats to study the biodistribution and accumulation of the magnetic particles in the major organs (Fig. 6E). The result suggested that the iron particles show no obvious accumulation in heart, liver, spleen, lung, and kidney and potentially have negligible side effects to the main organs. These results verified the in vivo therapeutic effect of MSCSMs, and the materials showed negligible side effects to the organisms.

DISCUSSION

We have developed a combined platform for the rapid deployment and high-precision delivery of the soft MSCSM to tortuous and tiny lumens that are with depth up to meter scale through a natural orifice and usually hard to reach by conventional surgical tools for therapeutic intervention. The developed MSCSMs are biohybrid and soft microrobots, with magnetic particles immobilized intercellularly. The MSCSMs have a highly saturated and compact cell arrangement with a maximum stem cell proportion of about 98% in volume. The MSCSMs inherit notable softness and biocompatibility of live tissue with a modulus comparable to that of human brain tissue, making the MSCSMs self-adaptable inside the body by alternating their morphologies in a reconfigurable fashion. The fabrication of MSCSMs has no adverse effects on stem cells, including cell viability, cell proliferation, and differentiation capacity. Moreover, the natural camouflage of the MSCSMs by the surface stem cells demonstrates the potential to suppress the immune response effectively. The long-term storage of MSCSMs is realized with high cell viability via a dynamic rotating culture system.

The whole-body scale deployment and delivery of soft microrobots are enabled by an integrated robotic platform, comprising a magnetic actuation unit, endoscope, and US imaging modality. For hard-to-reach regions that are inaccessible and even invisible to conventional endoscopes and medical robots, the developed EMADIS can actuate and deliver soft MSCSMs, with real-time tracking, to these sites with long navigation range and high targeting precision. As we know, the high-motion precision may result in a compromise of the delivery range. The proposed EMADIS is demonstrated to be an endoscopy/catheter-assisted microrobotic

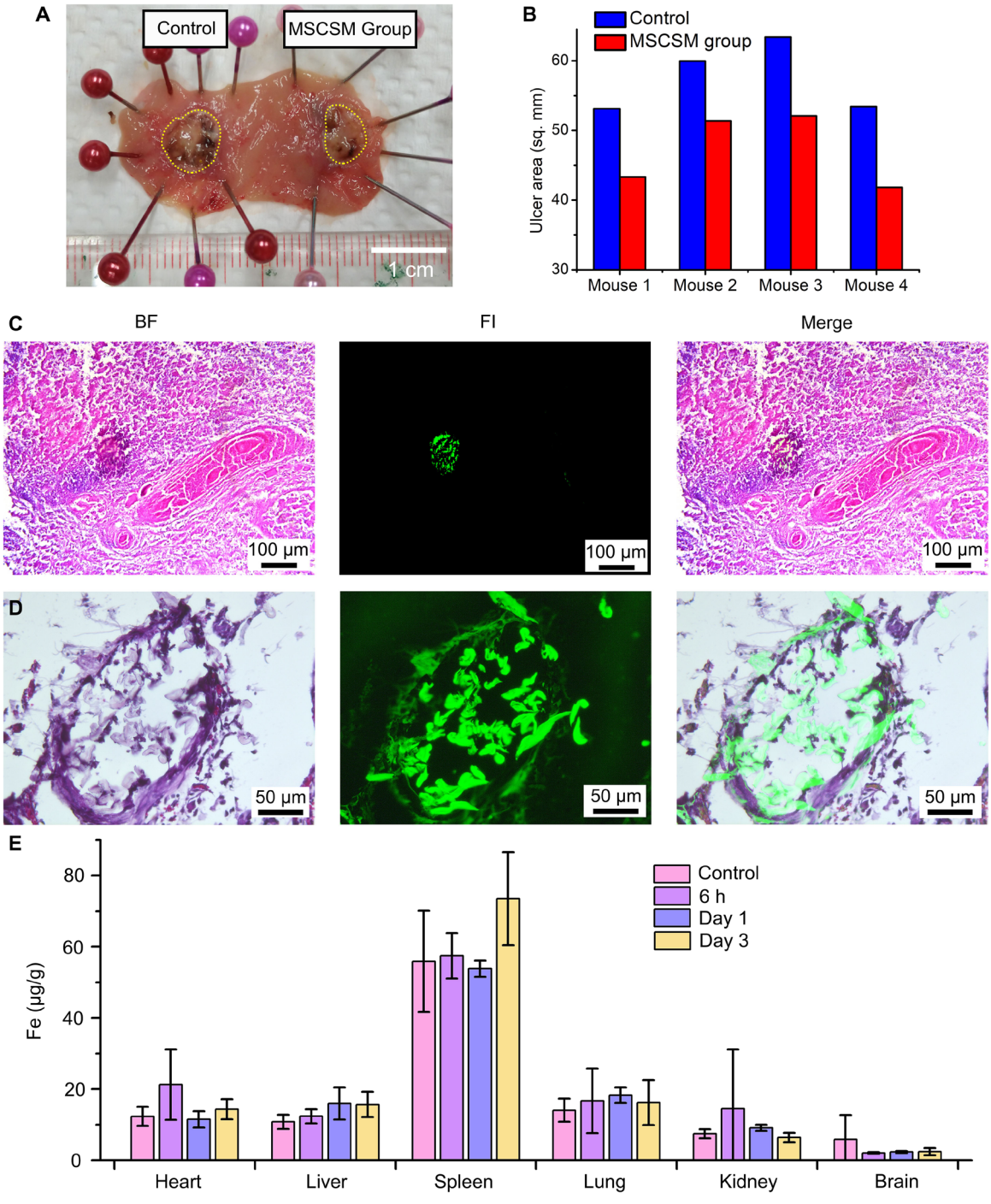

Fig. 6. Submucosal injection of MSCSMs promotes the healing of gastric ulcers in rats. (**A**) Macroscopic observation of gastric ulcers on day 3 in MSCSM group and control group. (**B**) Bar graph showing the surface areas of the gastric ulcer of the MSCSM group and control group (measured by ImageJ software). The healing rate of the gastric ulcers in MSCSM group after 3 days was higher than that in the control group. Paired *t* test showed $P < 0.001$. (**C**) H&E staining of the stomach tissue of the MSCSM group. (**D**) Enlarged views showing the released stem cells inside the stomach tissue. (**E**) In vivo biodistribution of Fe over 3 days in rats. Aliquots of the prepared magnetic particles were intravenously injected into the rats (dose = 60 mg/kg). The iron concentrations in the organs were determined at different time points after injection using ICP-OES. Error bars indicate the SD for $n \geq 3$.

platform for targeted active delivery across long distances with high precision and multiple organ barriers with high time efficiency. The precise delivery of MSCSMs by means of the EMADIS transesophageal into the bile duct with a total distance of about 100 cm can be completed within 8 min. In addition, the MSCSMs have also demonstrated exceptional in vivo therapeutic effects

on ulcer healing. As endoscopy techniques and microrobotics continue to advance, we envision that the integration of both aspects will lead to a promising therapeutic system with a highly extended working distance, improved time efficiency for remote delivery, and diverse functionalities with high clinical value.

MATERIALS AND METHODS

Materials

Carbonyl iron powder was purchased from Badische Anilin und Soda Fabrik (BASF). Dopamine hydrochloride was purchased from Aladdin Chemical Co. Ltd. Dulbecco's modified Eagle's medium (DMEM), fetal bovine serum (FBS), 0.25% trypsin-EDTA, 4′,6-diamidino-2-phenylindole, phosphate-buffered saline (PBS), and Nunclon Sphera 96-well U-shaped-bottom microplates were purchased from Gibco, Thermo Fisher Scientific. The MTS assay (ab197010) was purchased from Abcam. The 4% paraformaldehyde solution and Triton X-100 were purchased from Sigma-Aldrich. All chemicals were used as received without further purification.

Animal experiments in this study were carried out in accordance with the guidelines of the Animals Ordinance (Chapter 340), Department of Health, Hong Kong. All the procedures were approved by the Animal Experimentation Ethics Committee of the Chinese University of Hong Kong (CUHK).

Synthesis of PDA-coated magnetic microspheres

The PDA-coated magnetic microspheres were fabricated via a self-polymerization process on the surface of the carbonyl iron particles. Briefly, tris(hydroxymethyl)aminomethane solution with a concentration of 10 mM was prepared. The pH was tuned to 8.5 by using hydrochloric acid to form a tris-HCl buffer solution. The carbonyl iron particles (0.1 g) were dispersed in 50 ml of tris-HCl buffer solution using ultrasonic stirring. Then, 30 mg of dopamine hydrochloride was added to the suspension, and the mixture was subjected to 5 hours of ultrasonic and mechanical stirring in iced water bath. After that, the black product was collected by a magnet and washed with deionized water and ethanol five times. Last, the product was dispersed and stored in deionized water for further use.

Fabrication of MSCSMs

Adipose-derived mesenchymal stem cells (ADMSCs) were isolated from subcutaneous inguinal adipose tissue of male transgenic Sprague-Dawley rats expressing green fluorescent protein. Adherent ADMSCs were first grown to 80 to 90% confluence and were then detached by incubating the ADMSCs with a 0.25% trypsin-EDTA solution for 50 s at 37°C. Once the cells had detached from the dishes, trypsinization was stopped by immediately adding a double volume of DMEM supplemented with 10% FBS. The cell suspension was centrifuged at 1000 rpm for 5 min. The cell pellet was resuspended in 1 ml of DMEM containing 10% FBS, and the cell density was determined by means of a hemocytometer. ADMSC stock with a cell density of 1×10^6 cells/ml was prepared. Afterward, 100 μl of ADMSC stock solution was added to the nonadhesive 96-well plate. Then, magnetic particles with different doses were added to the ADMSC solutions in the nonadhesive 96-well plate. The 96-well plate was incubated at 37°C in a 5% CO_2 incubator for at least 1 day to generate MSCSMs. BF images were then captured using an inverted microscope.

Cell viability assay of MSCSMs

The MTS assay was used to evaluate the viability of MSCSMs. Briefly, MSCSMs with various particle concentrations and cell concentrations were cultured for 1 day. Twenty microliters of MTS solution and 100 μl of DMEM were added to each well. The MSCSMs were then cultured for 3 hours at 37°C in a 5% CO_2 incubator. Last, 100 μl of each sample solution was pipetted into a new 96-well plate. The absorbance at 490 nm was measured using a Tecan Infinite 200 PRO plate reader. All measurements were repeated at least three times. The cell viability of the MSCSMs without any particles was used as a control.

Differentiation of MSCSMs

In vitro differentiation of ADMSCs for osteogenesis and chondrogenesis was induced by using the differentiation medium from Gibco, Thermo Fisher Scientific. For chondrogenesis, Alcian blue was used to stain extracellular glycosaminoglycans. For osteogenesis, Alizarin Red S was used to detect calcium deposits.

Immunofluorescence staining

MSCSMs and stem cell spheroids were cultured in Nunclon Sphera 96 U-well plates. After different culture times, MSCSMs and stem cell spheroids were collected and transferred to a new 24-well plate. All cell samples were rinsed three times with a culture medium and then stained with Image-iT Red Hypoxia Reagent for 3 hours, followed by staining in NucBlue Live ReadyProbes Reagent for 20 min. After three washes with PBS, FIs were observed and captured using a Zeiss LSM 700 confocal laser scanning microscope. All staining procedures were conducted in a dark environment to avoid photobleaching.

Coculture with 3T3 spheroid microrobots

3T3 cells stock with a cell density of 1×10^6 cells/ml was prepared. Afterward, 100 μl of 3T3 stock solution was added into the nonadhesive 96-well plate with different doses of magnetic particles. The cells were incubated at 37°C in a 5% CO_2 incubator for at least 1 day to generate 3T3 spheroid microrobots. The cultured MSCSMs were transferred to the wells of the 3T3 spheroid microrobots and cultured for 5 days.

Cell spreading test

MSCSMs that were cultured for 1 day were rinsed three times with a culture medium to remove the loosely attached cells and were transferred to a new six-well plate. The MSCSMs were then cultured for 8 days. Optical images and fluorescence images were taken at different times using an inverted fluorescence microscope.

Cell engraftment assay

To evaluate the engraftment of MSCSMs, 3T3 cells were cultured in the largest well of the printed channel until confluent. Then, the cell monolayer was scratched using a 5-ml pipette tip in a straight line. Three MSCSMs were added to the far-end well without 3T3 cells. Afterward, the MSCSMs were delivered to the well with a 3T3 cell monolayer by means of a magnetic field and further placed on the scratched area. Images were acquired at 0, 21, and 30 hours. The scratched area was measured using ImageJ, and each experiment was repeated three times.

Cell migration assay

To evaluate the migration of 3T3 cells, 3T3 cells were cultured in the largest well of the printed channel until confluent. Then, the cell

monolayer was scratched using a 5-ml pipette tip in a straight line. The culture medium was changed to DMEM with 0.8% FBS. Twenty MSCSMs were added to the far-end well without 3T3 cells. Afterward, the MSCSMs were delivered to the well with a 3T3 cell monolayer by means of a magnetic field. Images were acquired at 0 and 15 hours. The scratched area was measured using ImageJ, and each experiment was repeated three times.

In vivo US tracking and actuation of MSCSMs

Female Sprague-Dawley rats weighing 200 to 250 g were used in this study. The rats were first anesthetized by an intraperitoneal injection of ketamine (80 mg/kg body weight) and xylazine (10 mg/kg body weight). Laparotomy was performed to expose the bladder. Twenty MSCSMs were injected into the bladder via a catheter near the ureter, and the wound was closed by suturing. The US probe was then placed on the rat's abdomen to image the urinary bladder and the MSCSMs inside.

T2-weighted in vitro and in vivo MRI

MRI was performed by means of a Philips Achieva TX 3.0T clinical scanner, equipped with a dual transmitter (Philips Healthcare, Best, the Netherlands) and a wrist coil as the radiofrequency transmitter and receiver, respectively. MSCSMs containing 0.02 mg of magnetic particles were prepared. They were transferred to 0.5-ml tubes and immersed in a water bath. They were then placed in the central part of the wrist coil. The samples were examined with a T2-weighted turbo spin echo (TSE) sequence in the coronal plane. For in vivo imaging, male adult C57 mice were used for this experiment. The mice were first anesthetized by an intraperitoneal injection of ketamine (80 mg/kg body weight) and xylazine (10 mg/kg body weight). MSCSMs were injected intraperitoneally via a 20-gauge catheter or delivered to the stomach by oral administration. The mouse was then placed in the supine position and the central part of the wrist coil. After the localization scan, the mouse was examined by means of a T2-weighted TSE sequence in the coronal plane. The parameters included repetition time/echo time = 4100/100 ms, in-plane resolution of 0.15 mm by 0.15 mm, slice thickness of 1 mm, echo train length of 10, flip angle of 900°, and number of signal averaging of 5. In addition, the magnetic field was applied to actuate the MSCSMs between two scans.

Endoscopy-assisted delivery of MSCSMs

Fresh pig stomach was purchased from the local market. An upper GI endoscope (GIF-HQ190; Olympus) was used in the experiment. First, the endoscope entered the pig's stomach via the esophagus. Then, a 14-gauge catheter was passed through the channel of the endoscope and reached inside the stomach. Fifteen MSCSMs were delivered to the stomach via the catheter by way of direct injection. The magnetic field setup then actuated the MSCSMs in the pig stomach.

In vivo gastric ulcer healing of MSCSMs

Male Sprague-Dawley rats weighing 200 to 250 g were used in this study. The gastric ulcer model of a rat was induced using acetic acid (*43*). Briefly, rats were fasted for 24 hours and then anesthetized by an intraperitoneal injection of ketamine (80 mg/kg body weight) and xylazine (10mg/kg body weight). Laparotomy was performed to expose the stomach. An incision was made at the fundus of the stomach. A hollow O-ring mold (OD of 10 mm) with an inlet and outlet was inserted into the stomach and pressed tightly with the fingers. Afterward, 75% acetic acid was injected into this mold, filling the mold completely for 70 s. Two "kissing" gastric ulcers were induced on the anterior and posterior walls of the stomach with identical sizes. Subsequently, 30 MSCSMs were injected via a 21-gauge catheter to the submucosa and subserosa around each ulcer. For the control group, 0.1 ml of saline was used and injected. The rats were euthanized on day 3 to harvest their stomach samples. The surface area of each gastric ulcer was measured using ImageJ. For histological evaluation, the specimens were fixed in 10% phosphate-buffered formalin for 24 hours. Five-micrometer sections of paraffin-embedded samples were deparaffinized and dehydrated. The slides were then washed twice with PBS, and H&E staining was performed. The histological analysis was conducted under a microscope to assess the healing of the gastric ulcer. Each experiment was repeated four times.

Characterization

Optical microscopy images were obtained using a HIROX RH-2000 microscope. SEM images were obtained using a JEOL JSM-7800F scanning electron microscope equipped with an x-ray energy-dispersive spectrometer (EDS) attachment. The specimens were sputtered with gold/platinum before SEM imaging. TEM images were captured using the JEOL Model JEM-2011 System equipped with an EDS attachment.

SUPPLEMENTARY MATERIALS

robotics.sciencemag.org/cgi/content/full/6/52/eabd2813/DC1

Supplementary Text

Fig. S1. Characterization of magnetic particles.

Fig. S2. High-resolution XPS spectra of the PDA coated magnetic particles.

Fig. S3. Optical images and FIs show the size and component of the MSCSMs.

Fig. S4. SEM images, EDS spectra, and enlarged SEM views showing the stem cell spheroids without and with magnetic particles.

Fig. S5. SEM images showing the inner structure of stem cells spheroid without the magnetic particles encapsulated inside, and the MSCSM with the magnetic particles.

Fig. S6. Cytotoxicity of different amounts of magnetic particles to the stem cells and 3T3 cells.

Fig. S7. Bar graph showing the comparison of the cytotoxicity of different amounts of pure magnetic particles and PDA functionalized magnetic particles.

Fig. S8. Long-term batch storage of the MSCSMs.

Fig. S9. Differentiation capability of the MSCSMs into different kinds of tiny cell robots.

Fig. S10. Generation of Janus cell microrobots with anisotropic structure or component.

Fig. S11. Potential aggregation of the magnetic particles during the magnetic actuation and digestion processes.

Fig. S12. Motion stability and fluorescence stability of the MSCSM with long-time locomotion under magnetic field.

Fig. S13. Motion of the MSCSMs on the surfaces with different viscosities.

Fig. S14. Motion of the MSCSMs on the surfaces with different wettabilities.

Fig. S15. Endoscopic delivery and locomotion of a swarm of MSCSMs in pig stomach.

Fig. S16. Successive BF, FI, and merged images showing the spreading and proliferation process of the MSCSM on a culture dish.

Fig. S17. Successive BF, FI, and merged images showing the spreading and proliferation process of the MSCSM on the 3T3 cell film.

Fig. S18. Optical images showing the spreading and proliferation process after the magnetic field actuated delivery on a culture dish.

Fig. S19. CLSM images showing stem cell configurations from the enlarged views of the center and edge of the spread MSCSM on a culture dish.

Fig. S20. Fluorescent images showing the spreading of two adjacent MSCSMs on a culture dish.

Fig. S21. US imaging-guided locomotion and delivery.

Fig. S22. MRI guided locomotion of MSCSMs.

Fig. S23. In vitro repairing of the scratched area and proliferation of MSCSMs on the scratches of 3T3 cell monolayers.

Fig. S24. MSCSMs enhanced the migration of 3T3 cells in vitro.

Table S1. Summary of the previous imaging methods during the biomedical applications of microrobots.

Table S2. The potential application regions of the proposed MSCSMs inside the body.
Table S3. Summary of different imaging modalities of microrobots towards in vivo applications.
Movie S1. Remote actuation of MSCSMs on tilted surfaces and against liquid flows using magnetic fields.
Movie S2. Controlled locomotion of MSCSMs in different surfaces and on-demand spreading and proliferation under the tracking of fluorescent imaging.
Movie S3. US imaging-guided actuation and delivery of MSCSMs.
Movie S4. Swarm locomotion of multiple MSCSMs on the uneven mucosa of pig stomach assisted by endoscopy.
Movie S5. Rapid and high-precision delivery of the MSCSMs transesophageal to the bile duct under combined imaging modalities in a real-time fashion by the EMADIS.
References (*44*–*58*)

REFERENCES AND NOTES

1. B. J. Nelson, I. K. Kaliakatsos, J. J. Abbott, Microrobots for minimally invasive medicine. *Annu. Rev. Biomed. Eng.* **12**, 55–85 (2010).
2. J. X. Li, B.-F. de Ávila, W. Gao, L. F. Zhang, J. Wang, Micro/nanorobots for biomedicine: Delivery, surgery, sensing, and detoxification. *Sci. Robot.* **2**, eaam6431 (2017).
3. W. Li, L. Y. Zhang, X. H. Ge, B. Y. Xu, W. X. Zhang, L. L. Qu, C.-H. Choi, J. H. Xu, A. Zhang, H. Lee, D. A. Weitz, Microfluidic fabrication of microparticles for biomedical applications. *Chem. Soc. Rev.* **47**, 5646–5683 (2018).
4. Z. G. Wu, L. Li, Y. R. Yang, P. Hu, Y. Li, S.-Y. Yang, L. V. Wang, W. Gao, A microrobotic system guided by photoacoustic computed tomography for targeted navigation in intestines in vivo. *Sci. Robot.* **4**, eaax0613 (2019).
5. Z. Wu, J. Troll, H.-H. Jeong, Q. Wei, M. Stang, F. Ziemssen, Z. Wang, M. Dong, S. Schnichels, T. Qiu, P. Fischer, A swarm of slippery micropropellers penetrates the vitreous body of the eye. *Sci. Adv.* **4**, eaat4388 (2018).
6. B. E.-F. de Ávila, P. Angsantikul, D. E. Ramírez-Herrera, F. Soto, H. Teymourian, D. Dehaini, Y. Chen, L. Zhang, J. Wang, Hybrid biomembrane–functionalized nanorobots for concurrent removal of pathogenic bacteria and toxins. *Sci. Robot.* **3**, eaat0485 (2018).
7. J. T. Kim, U. Choudhury, H.-H. Jeong, P. Fischer, Nanodiamonds that swim. *Adv. Mater.* **29**, 1701024 (2017).
8. T. G. Leong, C. L. Randall, B. R. Benson, N. Bassik, G. M. Stern, D. H. Gracias, Tetherless thermobiochemically actuated microgrippers. *Proc. Natl. Acad. Sci. U.S.A.* **106**, 703–708 (2009).
9. E. Gultepe, J. S. Randhawa, S. Kadam, S. Yamanaka, F. M. Selaru, E. J. Shin, A. N. Kalloo, D. H. Gracias, Biopsy with thermally-responsive untethered microtools. *Adv. Mater.* **25**, 514–519 (2013).
10. R. Cheng, W. J. Huang, L. J. Huang, B. Yang, L. D. Mao, K. L. Jin, Q. C. ZhuGe, Y. P. Zhao, Acceleration of tissue plasminogen activator-mediated thrombolysis by magnetically powered nanomotors. *ACS Nano* **8**, 7746–7754 (2014).
11. J. Shao, M. Abdelghani, G. Shen, S. Cao, D. S. Williams, J. C. M. van Hest, Erythrocyte membrane modified janus polymeric motors for thrombus therapy. *ACS Nano* **12**, 4877–4885 (2018).
12. J. Li, X. Li, T. Luo, R. Wang, C. Liu, S. Chen, D. Li, J. Yue, S.-h. Cheng, D. Sun, Development of a magnetic microrobot for carrying and delivering targeted cells. *Sci. Robot.* **3**, eaat8829 (2018).
13. S. Tang, F. Zhang, H. Gong, F. Wei, J. Zhuang, E. Karshalev, B. E.-F. de Ávila, C. Huang, Z. Zhou, Z. Li, L. Yin, H. Dong, R. H. Fang, X. Zhang, L. Zhang, J. Wang, Enzyme-powered Janus platelet cell robots for active and targeted drug delivery. *Sci. Robot.* **5**, eaba6137 (2020).
14. M. Medina-Sánchez, L. Schwarz, A. K. Meyer, F. Hebenstreit, O. G. Schmidt, Cellular cargo delivery: Toward assisted fertilization by sperm-carrying micromotors. *Nano Lett.* **16**, 555–561 (2016).
15. L. Ricotti, B. Trimmer, A. W. Feinberg, R. Raman, K. K. Parker, R. Bashir, M. Sitti, S. Martel, P. Dario, A. Menciassi, Biohybrid actuators for robotics: A review of devices actuated by living cells. *Sci. Robot.* **2**, eaaq0495 (2017).
16. J. Yu, D. Jin, K.-F. Chan, Q. Wang, K. Yuan, L. Zhang, Active generation and magnetic actuation of microrobotic swarms in bio-fluids. *Nat. Commun.* **10**, 5631 (2019).
17. X. Yan, Q. Zhou, M. Vincent, Y. Deng, J. Yu, J. Xu, T. Xu, T. Tang, L. Bian, Y.-X. Wang, K. Kostarelos, L. Zhang, Multifunctional biohybrid magnetite microrobots for imaging-guided therapy. *Sci. Robot.* **2**, eaaq1155 (2017).
18. S. Jeon, S. Kim, S. Ha, S. Lee, E. Kim, S. Y. Kim, S. H. Park, J. H. Jeon, S. W. Kim, C. Moon, B. J. Nelson, J.-y. Kim, S.-W. Yu, H. Choi, Magnetically actuated microrobots as a platform for stem cell transplantation. *Sci. Robot.* **4**, eaav4317 (2019).
19. O. Felfoul, M. Mohammadi, S. Taherkhani, D. de Lanauze, Y. Z. Xu, D. Loghin, S. Essa, S. Jancik, D. Houle, M. Lafleur, L. Gaboury, M. Tabrizian, N. Kaou, M. Atkin, T. Vuong, G. Batist, N. Beauchemin, D. Radzioch, S. Martel, Magneto-aerotactic bacteria deliver drug-containing nanoliposomes to tumour hypoxic regions. *Nat. Nanotechnol.* **11**, 941–947 (2016).
20. S. Martel, O. Felfoul, J.-B. Mathieu, A. Chanu, S. Tamaz, M. Mohammadi, M. Mankiewicz, N. Tabatabaei, MRI-based Medical nanorobotic platform for the control of magnetic nanoparticles and flagellated bacteria for target interventions in human capillaries. *Int. J. Rob. Res.* **28**, 1169–1182 (2009).
21. Y. Zhang, L. Zhang, L. Yang, C. I. Vong, K. F. Chan, W. K. K. Wu, T. N. Y. Kwong, N. W. S. Lo, M. Ip, S. H. Wong, J. J. Y. Sung, P. W. Y. Chiu, L. Zhang, Real-time tracking of fluorescent magnetic spore–based microrobots for remote detection of C. *diff* toxins. *Sci. Adv.* **5**, eaau9650 (2019).
22. Y. Zhang, K. Yan, F. Ji, L. Zhang, Enhanced removal of toxic heavy metals using swarming biohybrid adsorbents. *Adv. Funct. Mater.* **28**, 1806340 (2018).
23. X. Wang, X.-H. Qin, C. Hu, A. Terzopoulou, X.-Z. Chen, T.-Y. Huang, K. Maniur-Weber, S. Pané, B. J. Nelson, 3D printed enzymatically biodegradable soft helical microswimmers. *Adv. Funct. Mater.* **28**, 1804107 (2018).
24. B. Wang, K. F. Chan, J. Yu, Q. Wang, L. Yang, P. W. Y. Chiu, L. Zhang, Reconfigurable swarms of ferromagnetic colloids for enhanced local hyperthermia. *Adv. Funct. Mater.* **28**, 1705701 (2018).
25. J. Yu, B. Wang, X. Du, Q. Wang, L. Zhang, Ultra-extensible ribbon-like magnetic microswarm. *Nat. Commun.* **9**, 3260 (2018).
26. S. Palagi, P. Fischer, Bioinspired microrobots. *Nat. Rev. Mater.* **3**, 113–124 (2018).
27. B. E.-F. de Ávila, P. Angsantikul, J. Li, W. Gao, L. Zhang, J. Wang, Micromotors Go In Vivo: From test tubes to live animals. *Adv. Funct. Mater.* **28**, 1705640 (2018).
28. M. Sitti, H. Ceylan, W. Hu, J. Giltinan, M. Turan, S. Yim, E. Diller, Biomedical applications of untethered mobile milli/microrobots. *Proc. IEEE* **103**, 205–224 (2015).
29. J. F. Schenck, Safety of strong, static magnetic fields. *J. Magn. Reson. Imaging* **12**, 2–19 (2000).
30. C. Laschi, B. Mazzolai, M. Cianchetti, Soft robotics: Technologies and systems pushing the boundaries of robot abilities. *Sci. Robot.* **1**, eaah3690 (2016).
31. M. Medina-Sánchez, V. Magdanz, M. Guix, V. M. Fomin, O. G. Schmidt, Swimming microrobots: Soft, reconfigurable, and smart. *Adv. Funct. Mater.* **28**, 1707228 (2018).
32. H.-W. Huang, M. S. Sakar, A. J. Petruska, S. Pané, B. J. Nelson, Soft micromachines with programmable motility and morphology. *Nat. Commun.* **7**, 12263 (2016).
33. Y. Morimoto, H. Onoe, S. Takeuchi, Biohybrid robot powered by an antagonistic pair of skeletal muscle tissues. *Sci. Robot.* **3**, eaat4440 (2018).
34. Y. Kim, G. A. Parada, S. Liu, X. Zhao, Ferromagnetic soft continuum robots. *Sci. Robot.* **4**, eaax7329 (2019).
35. J. Liu, S. Lin, X. Zhao, Hydrogel machines. *Mater. Today* **36**, 102–124 (2020).
36. X. Yang, W. Shang, H. Lu, Y. Liu, L. Yang, R. Tan, X. Wu, Y. Shen, An agglutinate magnetic spray transforms inanimate objects into millirobots for biomedical applications. *Sci. Robot.* **5**, eabc8191 (2020).
37. X. Zhao, Y. Kim, Soft microbots controlled by nanomagnets. *Nature* **575**, 58–59 (2019).
38. M. Sitti, Miniature soft robots — Road to the clinic. *Nat. Rev. Mater.* **3**, 74–75 (2018).
39. M. S. Medina-Sánchez, O. G. Schmidt, Medical microbots need better imaging and control. *Nature* **545**, 406–408 (2017).
40. H. Deng, X. L. Li, Q. Peng, X. Wang, J. Chen, Y. D. Li, Monodisperse magnetic single-crystal ferrite microspheres. *Angew. Chem. Int. Ed.* **44**, 2782–2785 (2005).
41. D. T. Butcher, T. Alliston, V. M. Weaver, A tense situation: Forcing tumour progression. *Nat. Rev. Cancer* **9**, 108–122 (2009).
42. A. M. Handorf, Y. Zhou, M. A. Halanski, W.-J. Li, Tissue stiffness dictates development, homeostasis, and disease progression. *Organogenesis* **11**, 1–15 (2015).
43. S. Okabe, K. Amagase, An overview of acetic acid ulcer models--the history and state of the art of peptic ulcer research. *Biol. Pharm. Bull.* **28**, 1321–1341 (2005).
44. H. Xu, M. Medina-Sánchez, V. Magdanz, L. Schwarz, F. Hebenstreit, O. G. Schmidt, Sperm-hybrid micromotor for targeted drug delivery. *ACS Nano* **12**, 327–337 (2018).
45. G. Go, S.-G. Jeong, A. Yoo, J. Han, B. Kang, S. Kim, K. T. Nguyen, Z. Jin, C.-S. Kim, Y. R. Seo, J. Kang, J. Y. Na, E. K. Song, Y. Jeong, J. K. Seon, J.-O. Park, E. Choi, Human adipose–derived mesenchymal stem cell–based medical microrobot system for knee cartilage regeneration in vivo. *Sci. Robot.* **5**, eaay6626 (2019).
46. B.-W. Park, J. Zhuang, O. Yasa, M. Sitti, Multifunctional bacteria-driven microswimmers for targeted active drug delivery. *ACS Nano* **11**, 8910–8923 (2017).
47. J. Li, S. Thamphiwatana, W. Liu, B. E.-F. de Ávila, P. Angsantikul, E. Sandraz, J. Wang, T. Xu, F. Soto, V. Ramez, X. Wang, W. Gao, L. Zhang, J. Wang, Enteric micromotor can selectively position and spontaneously propel in the gastrointestinal tract. *ACS Nano* **10**, 9536–9542 (2016).
48. E. Karshalev, B. E.-F. de Ávila, M. Beltrán-Gastélum, P. Angsantikul, S. Tang, R. Mundaca-Uribe, F. Zhang, J. Zhao, L. Zhang, J. Wang, Micromotor pills as a dynamic oral delivery platform. *ACS Nano* **12**, 8397–8405 (2018).

49. A. Servant, F. M. Qiu, M. Mazza, K. Kostarelos, B. J. Nelson, Controlled in vivo swimming of a swarm of bacteria-like microrobotic flagella. *Adv. Mater.* **27**, 2981–2988 (2015).
50. J. Hu, S. Huang, L. Zhu, W. Huang, Y. Zhao, K. Jin, Q. ZhuGe, Tissue plasminogen activator-porous magnetic microrods for targeted thrombolytic therapy after ischemic stroke. *ACS Appl. Mater. Interfaces* **10**, 32988–32997 (2018).
51. J. R. Baylis, J. H. Yeon, M. H. Thomson, A. Kazerooni, X. Wang, A. E. St. John, E. B. Lim, D. Chien, A. Lee, J. Q. Zhang, J. M. Piret, L. S. Machan, T. F. Burke, N. J. White, C. J. Kastrup, Self-propelled particles that transport cargo through flowing blood and halt hemorrhage. *Sci. Adv.* **1**, e1500379 (2015).
52. W. He, J. Frueh, N. Hu, L. Liu, M. Cai, Q. He, Guidable thermophoretic janus micromotors containing gold nanocolorifiers for infrared laser assisted tissue welding. *Adv. Sci.* **3**, 1600206 (2016).
53. J. Pokki, O. Ergeneman, G. Chatzipirpiridis, T. Lühmann, J. Sort, E. Pellicer, S. A. Pot, B. M. Spiess, S. Pané, B. J. Nelson, Protective coatings for intraocular wirelessly controlled microrobots for implantation: Corrosion, cell culture, and in vivo animal tests. *J. Biomed. Mater. Res. B Appl. Biomater.* **105**, 836–845 (2017).
54. Q. Wang, L. Yang, J. Yu, P. W. Y. Chiu, Y.-P. Zheng, L. Zhang, Real-time magnetic navigation of a rotating colloidal microswarm under ultrasound guidance. *IEEE Trans. Biomed. Eng.* **67**, 3403–3412 (2020).
55. S. Kim, F. Qiu, S. Kim, A. Ghanbari, C. Moon, L. Zhang, B. J. Nelson, H. Choi, Fabrication and characterization of magnetic microrobots for three-dimensional cell culture and targeted transportation. *Adv. Mater.* **25**, 5863–5868 (2013).
56. V. Magdanz, S. Sanchez, O. G. Schmidt, Development of a sperm-flagella driven micro-bio-robot. *Adv. Mater.* **25**, 6581–6588 (2013).
57. B. E.-F. de Ávila, C. Angell, F. Soto, M. A. Lopez-Ramirez, D. F. Báez, S. Xie, J. Wang, Y. Chen, Acoustically propelled nanomotors for intracellular siRNA delivery. *ACS Nano* **10**, 4997–5005 (2016).
58. S. Scheggi, K. K. T. Chandrasekar, C. Yoon, B. Sawaryn, G. Steeg, D. H. Gracias, S. Misra, Magnetic motion control and planning of untethered soft grippers using ultrasound image feedback, in *2017 IEEE International Conference on Robotics and Automation (ICRA)* 6156–6161 (2017).

Acknowledgments: We thank F. Ji and S. Kou from CUHK for the assistance in simulation and inductively coupled plasma optical emission spectrometer (ICP-OES) characterization, respectively. **Funding:** This work was partially supported by the Hong Kong RGC Joint Laboratory Funding Scheme (JLFS) with project no. JLFS/E-402/18; the projects funded by the Hong Kong ITC with project numbers MRP/036/18X, ITS/440/17FP, and ITS/374/18FP; the projects from CUHK internal grants; and the support from SIAT-CUHK Joint Laboratory of Robotics and Intelligent Systems. B.W. thanks the financial support from the Impact Postdoctoral Fellowship Scheme from the Chinese University of Hong Kong. We would also like to thank the support from Multi-Scale Medical Robotics Center (MRC), InnoHK, at the Hong Kong Science Park. **Author contributions:** B.W., K.F.C., and L.Z. designed the processing approach. B.W. and K.F.C. conducted the experiments and wrote the manuscript with input from the other authors. L.Z. mentored the work and revised the manuscript. K.F.C. and B.W. performed the cell related experiments. K.F.C., B.W., K.Y., Q.W., and X.X. conducted the ex vivo experiments in GI tract and in vivo experiments in rat. J.J.Y.S., P.W.Y.C., and H.K. contributed to the discussion of the animal experiments. L.Y. supported the automated motion experiments. B.W., K.F.C. and Y.-X.J.W. conducted the MR imaging experiment. All the authors provided suggestions and revised the manuscript. **Competing interests:** L.Z., B.W., K.F.C., and P.W.Y.C. are inventors with a U.S. Provisional Patent (U.S. application no. 63/040,049, filed on 17 June 2020) on the integrated robotic platform for rapid endoluminal delivery of miniature robots. The other authors declare that they have no competing interests. **Data and materials availability:** All data needed to evaluate the conclusions in the paper are present in the paper or the Supplementary Materials.

Submitted 11 June 2020
Accepted 16 February 2021
Published 17 March 2021
10.1126/scirobotics.abd2813

Citation: B. Wang, K. F. Chan, K. Yuan, Q. Wang, X. Xia, L. Yang, H. Ko, Y.-X. J. Wang, J. J. Y. Sung, P. W. Y. Chiu, L. Zhang, Endoscopy-assisted magnetic navigation of biohybrid soft microrobots with rapid endoluminal delivery and imaging. *Sci. Robot.* **6**, eabd2813 (2021).

Science Robotics

Endoscopy-assisted magnetic navigation of biohybrid soft microrobots with rapid endoluminal delivery and imaging

Ben Wang, Kai Fung Chan, Ke Yuan, Qianqian Wang, Xianfeng Xia, Lidong Yang, Ho Ko, Yi-Xiang J. Wang, Joseph Jao Yiu Sung, Philip Wai Yan Chiu, and Li Zhang

Sci. Robot. **6** (52), eabd2813. DOI: 10.1126/scirobotics.abd2813

Science Robotics (ISSN 2470-9476) is published by the American Association for the Advancement of Science. 1200 New York Avenue NW, Washington, DC 20005. The title *Science Robotics* is a registered trademark of AAAS.